Effect of Bed Clay on Surface Water-Wave Reconstruction from Ripples

Jonathan Malarkey[1], Ellen M. Pollard[2], Roberto Fernández[3], Xuxu Wu[2,4], Jaco H. Baas[1] and Daniel R. Parsons[5]

[1]School of Ocean Sciences, Bangor University, Menai Bridge, Anglesey LL59 5AB, UK.

[2]Energy and Environment Institute, University of Hull, Hull, HU6 7RX, UK.

[3]Department of Civil and Environmental Engineering, The Pennsylvania State University, State College, PA 16802, USA.

[4]School of Environmental Sciences, University of Hull, Hull, HU6 7RX, UK.

[5]Department of Geography and Environment, Loughborough University, Loughborough, LE11 3TU, UK.

Corresponding author: Jonathan Malarkey (j.malarkey@bangor.ac.uk)

Key Points:

- Wave-ripple dimensions provide important information on past subaqueous environments
- Here, a clean-sand method is adapted for clay-sand mixtures by incorporating the effect of changes in the threshold of motion and dimensions
- Clay can result in a reduction in the range of past water-surface wavelengths and water depths, which is largest for coarse sand

Abstract

Wave ripples can provide valuable information on their formative hydrodynamic conditions in past subaqueous environments by inverting dimension predictors. However, these inversions do not usually take the mixed non-cohesive and cohesive nature of sediment beds into account. Recent experiments involving sand–kaolinite mixtures have demonstrated that wave-ripple dimensions and the threshold of motion are affected by bed clay content. Here, a clean-sand method to determine wave climate based on orbital ripple wavelength has been adapted to include the effect of clay and a consistent shear-stress threshold parameterisation. Based on present-day examples with known wave conditions, the results show that the largest clay effect occurs for coarse sand with median grain diameters over 0.45 mm. For a 7.4% volumetric clay concentration, the range of possible water-surface wavelengths and water depths can be reduced significantly, by a factor of three and four, respectively, compared to clean sand.

Plain Language Summary

In shallow water, ripples form on the seabed under water-surface waves due to friction. Knowledge of this process allows preserved ripples to be used to infer past environmental conditions. Traditionally, the method of inferring past environments from wave ripples has only involved sand, despite mixtures of sand and sticky mud being more common in nature. Based on the results of recent mixed sand–mud experiments, the effect of including small amounts of mud in the analysis is shown to be an important modifying factor in determining past environments.

1 Introduction

Bed-surface structures in sediments and sedimentary rocks of past subaqueous environments provide important information on flow hydraulics (e.g. Collinson & Mountney, 2019). These structures tend to be classified on the basis of the presence or absence of cohesion in equivalent modern environments: (a) cohesive structures, associated with physical cohesion by clay particles and biological cohesion by extracellular polymeric substances (e.g. biofilms, Vignaga et al., 2013), where the bed is stabilised by cohesion between grains and sudden catastrophic failure may occur under high bed shear stress, e.g. during storms; and (b) non-cohesive bedforms (e.g. wave and current ripples: Wiberg & Harris, 1994; Baas, 1994), where grains can move individually and tend to respond more rapidly and continuously to changes in flow forcing (Perron et al., 2018). Examples of these types of bed-surface structure include roll-ups (Cuadrado, 2020) and non-cohesive wave ripples (e.g. Allen, 1981). Davies (2016) argued that the distinction between cohesive and non-cohesive sedimentary structures is artificial, as they represent end members of a spectrum, and thus predictions based on one classification may result in misinterpretations. This position is re-enforced by recent experiments that have shown how sandy bedforms can be affected by small amounts of biological and physical cohesion (Malarkey et al., 2015; Parsons et al., 2016; Wu et al., 2018; 2022). The consequence for wave ripples of physical cohesion associated with kaolin clay in the bed has been detailed by Wu et al. (2024). Building on the work of Allen (1981), Diem (1985) developed a clean-sand analytical method for the prediction of paleowave climate based on the dimensional measurement of wave ripples in the rock record (Aspler et al., 1994; Wetzel et al., 2003; Allen & Hoffman, 2005; Pochat & Van Den Driessche, 2011, Lamb et al., 2012). Here, Diem's (1985) approach is adapted for sand–clay mixtures, using the synthesis proposed by Wu et al. (2024).

60   Diem's (1985) approach starts by determining the wave orbital diameter from the ripple
61 wavelength, without requiring a specific wavelength predictor. Here, the formulation starts as
62 Diem (1985) did, with linear wave theory and additional constraints based on threshold of motion
63 and wave breaking. It will then return to the effect of clay on ripple-wavelength prediction and the
64 threshold of motion. The importance of clay content is demonstrated with the use of present-day
65 examples from the laboratory and field, where the wave conditions were known.

66 **2 Diem's (1985) method**

67 2.1 Linear wave theory

68 In linear wave theory, the dispersion relation and the wave-velocity amplitude, U_0, are

$$\sigma^2 = gk\tanh kh, \quad U_0 = \pi d_0/T, \qquad (1a,b)$$

69 where $\sigma = 2\pi/T$, T is the wave period, g is the acceleration due to gravity ($= 9.81$ m s^{-2}), $k = 2\pi/L$,
70 L is the water-surface wavelength, h is the water depth, d_0 is the orbital diameter ($= H/\sinh kh$) and
71 H is the wave height. The wave properties, characterised by eqs. (1a,b), are subject to two
72 constraints:

73 2.1.1 Threshold of motion

74 U_t, the critical wave-velocity amplitude associated with the threshold of motion, is a function of
75 d_0 and D_{50}, the median grain diameter. For sediment movement $U_0^2 > U_t^2$, which when combined
76 with eqs. (1a,b) gives

$$x < \tanh kh, \qquad (2)$$

77 where $x = L/L_{t\infty}$ and $L_{t\infty} = \frac{1}{2}\pi g(d_0/U_t)^2$ is the deep-water surface wavelength corresponding to the
78 threshold of motion.

79 2.1.2 Wave breaking

80 According to Miche (1944), the wave-breaking criterion defines the maximum possible wave
81 steepness as, $H/L \leq 0.142\tanh kh$, which when combined with d_0 and $L_{t\infty}$ gives

$$x \geq A\cosh kh, \qquad (3)$$

82 where $A = d_0/0.142L_{t\infty} = U_t^2/(0.071\pi g d_0)$. It will be shown below that $A < \frac{1}{2}$, so if $A = \frac{1}{2}(U_t/U_m)^2$,
83 where $U_m = (0.0355\pi g d_0)^{\frac{1}{2}}$ is the maximum wave-velocity amplitude ($U_m > U_t$), then $U_t < U_0 \leq U_m$
84 and from eq. (1b) $\pi d_0/U_m \leq T < \pi d_0/U_t$.

85 Eqs. (2) and (3) represent the range of possible conditions between threshold and wave breaking
86 for the wave climate. The limits of these constraints can be found by combining eqs. (2) and (3)
87 using the identity $1-\tanh^2 kh = \text{sech}^2 kh$, such that the maximum and minimum in x satisfy the
88 equation $x^4 - x^2 + A^2 = 0$, so that $x_{\max,\min}$ are

$$x_{\max,\min} = [\frac{1}{2} \pm \frac{1}{2}(1 - 4A^2)^{\frac{1}{2}}]^{\frac{1}{2}}, \qquad (4)$$

89 where $A < \frac{1}{2}$, for there to be two distinct values. Here, x and kh are in the ranges $x_{\min} \leq x < x_{\max}$
90 and $\text{arctanh}\,x < kh \leq \text{arccosh}(x/A)$, respectively.

91 Figure 1 shows kh versus x for the limiting single-value case where $U_m^2 = U_t^2$ ($A = \frac{1}{2}$, $x = 2^{-\frac{1}{2}}$ and
92 $kh = \text{arctanh}\,2^{-\frac{1}{2}} \sim 0.88$) from shallow water ($kh \ll 1$) to deep water ($kh \gg 1$). Figure 1 also shows

93 the $A = \frac{1}{4}$ case ($U_m^2 = 2U_t^2$), corresponding to typical above-threshold wave conditions. In the
94 latter case, the shaded region in Figure 1 shows the allowable values of x ($\frac{1}{4}\cosh kh \leq x < \tanh kh$)
95 and the dots mark $x_{\mathrm{max,min}} = \frac{1}{2}(2\pm3^{1/2})^{1/2}$ and $kh_{\mathrm{max,min}} = \mathrm{arctanh}(x_{\mathrm{max,min}})$. The breaking-wave curves
96 ($x = A\cosh kh$) are concave downward and the threshold curve ($x = \tanh kh$) is concave upward.
97 Notice for the breaking-wave curves, $x \to A$ for $kh \ll 1$ and A also controls the slope for larger kh.
98 In dimensional terms, the water-surface wavelength, L, is therefore limited by the threshold scale
99 ($L_{t\infty}$) and breaking-wave scale ($AL_{t\infty}$) according to $AL_{t\infty} < L \leq L_{t\infty}$. Then, from eqs. (2) and (3), the
100 range of h can be expressed as a function of L as

$$(L/2\pi)\mathrm{arctanh}(L/L_{t\infty}) \leq h \leq (L/2\pi)\mathrm{arccosh}(L/AL_{t\infty}). \tag{5}$$

101 ## 2.2 The ripple predictor

102 Diem's (1985) central assumption is that the orbital diameter can be expressed in terms of an
103 equilibrium ripple wavelength, λ_e, as

$$\lambda_e = \alpha_0 d_0, \tag{6}$$

104 where $\alpha_0 = 0.65$, based on Miller and Komar's (1980) experiments, provided that $\lambda_e < 200$ mm (d_0
105 $= 308$ mm). Above this limit, Diem (1985) proposed the use of Sleath's (1975) predictor. This
106 arbitrary 200-mm limit represents the lower boundary of the suborbital and anorbital ranges, where
107 the wavelength is dependent on both d_0 and D_{50} for suborbital ripples and only dependent on D_{50}
108 for anorbital ripples. However, while a value of α_0 in the range $0.5 \leq \alpha_0 \leq 0.75$ in eq. (6) is widely
109 accepted, there is little agreement in the literature on the precise nature of the orbital, suborbital,
110 and anorbital limits. Wiberg and Harris (1994) defined orbital, suborbital and anorbital ripples by
111 $d_0/D_{50} \leq 1754$, $1754 < d_0/D_{50} \leq 5587$ and $d_0/D_{50} > 5587$, respectively (Malarkey & Davies, 2003),
112 whereas Mogridge et al. (1994) and Pedocchi and García (2009) argued the anorbital limit should
113 have wave-period dependence. Provided that eq. (6) *does* hold, which is what will be assumed
114 here, all quantities involving d_0 can now be expressed in terms of λ_e.

115 **3 Adaptions to Diem's (1985) method**

116 ## 3.1 Threshold of motion parameterisation

117 Based on Soulsby's (1997) critical threshold of motion for clean sand, Appendix A derives an
118 expression for U_t^2, eq. (A2), such that U_t^2, $L_{t\infty}$ and $AL_{t\infty}$ can be written

$$U_t^2 = B(gd_0^{0.52}D_{50}^{0.48}), \quad L_{t\infty} = \frac{\pi}{2B}\left(\frac{d_0^{1.48}}{D_{50}^{0.48}}\right), \quad AL_{t\infty} = \frac{d_0}{0.142}, \tag{7a,b,c}$$

119 where $B = 3.653(s-1)\theta_0$, s is the relative density of sediment in water (eq. A1), θ_0 is the critical
120 skin friction Shields parameter (eq. A1), and $d_0 = \lambda_e/\alpha_0$ from eq. (6). Diem (1985) used Komar and
121 Miller's (1973) mobility threshold prescription. Here, Soulsby's expression has been used, as it
122 allows U_t^2 to be directly related to θ_0 and it avoids the need for two different functional forms, for
123 $D_{50} < 0.5$ mm and $D_{50} \geq 0.5$ mm (eqs. (B1) and (B2)).

124 ## 3.2 Inclusion of the effect of clay

125 Wu et al. (2024) showed that the ratio of wavelength to orbital diameter, α, which replaces α_0 in
126 eq. (6), can be expressed as

$$\alpha = \alpha_0 \times \begin{cases} 1, & C_0 \le C_{0m}, \\ 1 - 5.5(C_0 - C_{0m}), & C_0 > C_{0m}, \end{cases} \tag{8}$$

where α_0 is the clean-sand constant of proportionality ($= 0.61$), C_0 is the clay content in the bed and $C_{0m} = 7.4\%$ is the minimum value of C_0 where α can change from α_0, and $\alpha = \tfrac{1}{2}\alpha_0$ for $C_0 = 16.3\%$. Whitehouse et al. (2000) showed that the threshold of motion is enhanced by the clay content according to

$$\theta_{0E} = \theta_0 B_\theta, \tag{9}$$

where θ_0 is the clean-sand threshold, $B_\theta = 1 + P_\theta C_0$ and P_θ is a constant that depends on the sediment properties. Based on their experiments, Wu et al. (2024) determined that $P_\theta = 6.3$ for $D_{50} = 0.143$ mm and $P_\theta = 23$ for $0.45 \le D_{50} \le 0.5$ mm (between these two ranges, it will be assumed that P_θ can be linearly interpolated). Notice in eq. (9) that even small amounts of clay produce an enhancement which is strongly dependent on grain size.

Thus, the two main effects of including clay are that α is reduced and θ_{0E} is increased. Substituting eqs. (8) and (9), into eqs. (7a,b,c) gives U_t^2, $L_{t\infty}$ and $AL_{t\infty}$ as

$$U_t^2 = B\left[\frac{B_\theta}{\alpha^{0.52}}\right](g\lambda_e^{0.52}D_{50}^{0.48}), \quad L_{t\infty} = \frac{\pi}{2B[B_\theta\alpha^{1.48}]}\left(\frac{\lambda_e^{1.48}}{D_{50}^{0.48}}\right), \quad AL_{t\infty} = \frac{\lambda_e}{0.142[\alpha]}, \tag{10a,b,c}$$

where λ_e is the mixed clay–sand ripple wavelength and only the square-bracketed quantity in each expression depends on C_0.

3.3 The method

The method begins with the determination of the ripple wavelength, λ_e, and bed-clay content, C_0. Once these have been determined, the following calculations are undertaken:

(i) Use λ_e and C_0 in eqs. (10a,b,c), with α and B_θ given by eqs. (8) and (9), to determine U_t, $L_{t\infty}$ and $AL_{t\infty}$

(ii) Use A in eq. (4) to determine $x_{\max,\min}$, so that $x_{\min} \le x \le x_{\max}$

(iii) Use $L = L_{t\infty}x$ to determine the range of h based on eq. (5) and U_t and $U_m = (0.0355\pi g\lambda_e/\alpha)^{1/2}$ to determine the ranges of U_0 and T: $U_t < U_0 < U_m$ and $\pi\lambda_e/\alpha U_m < T < \pi\lambda_e/\alpha U_t$

4 Example cases

With specific examples from the rock record, Diem (1985) was able to show how local considerations and context could be used to further limit the theoretical ranges described in the previous section. Here, modern-day examples, where the wave properties are known, are used, so that attention can be focussed on the effect of clay on the theoretical ranges alone. The example cases correspond to clean, coarse-, medium- and fine-grained sand from the laboratory and field, and involve determining how wave conditions based on the measured ripples change if the clay content is varied in the range $0 \le C_0 \le 16.3\%$.

4.1 Wu et al. (2018), coarse-sand laboratory data

Wu et al. (2018) conducted a series of experiments involving a single-wave condition over a bed composed of well-sorted coarse sand, $D_{50} = 0.496$ mm ($\theta_0 = 0.032$), and varying clay content, $0 \le C_0 \le 7.4\%$. For the clean sand experiment ($C_0 = 0\%$), the wave conditions were given by $h = 0.6$

160 m, $H = 0.16$ m and $T = 2.49$ s ($L = 5.62$ m), corresponding to $d_0 = 0.223$ m. This experiment
161 produced ripples with a wavelength $\lambda_e = 278D_{50}$ (Wu et al., 2024). Figure 2a show the threshold
162 and wave-breaking scales, $L_{t\infty}$ and $AL_{t\infty}$, versus C_0. $L_{t\infty}$, which is smallest at $C_0 = 7.4\%$, has a much
163 larger range than $AL_{t\infty}$, which is constant for $C_0 \leq 7.4\%$ and then doubles up to $C_0 = 16.3\%$. Figure
164 2d shows the corresponding L-h phase space, based on eq. (5), for the clay contents depicted in
165 Figure 2a ($C_0 = 0$, 7.4 and 16.3%). Compared to the dimensionless x–kh plot (Figure 1), the
166 threshold curves are still concave downwards, but more exaggerated, and the breaking-wave
167 curves are close to straight lines. The change in ranges is largely due to changes in $L_{t\infty}$. The
168 reduction in range between the largest and smallest (corresponding to $C_0 = 0\%$ and 7.4%) is by a
169 factor of 3 and 4 for the water-surface wavelength and water depth, respectively (Figure 2d).
170 Notice that the actual surface wavelength and water depth ($L = 5.62$ m, $h = 0.6$ m) are within all
171 three ranges. Figures 2a,d can be compared with Figures B1a,b to see the effect of using the Komar
172 and Miller (1973) clean-sand mobility description for the threshold. This shows $L_{t\infty}$ to be about
173 63% of its value in Figure 2a, because $B = 0.21(s{-}1) = 0.34$ as opposed to $3.653(s{-}1)\theta_0 = 0.19$.
174 Thus, using Diem's (1985) clean-sand mobility description underpredicts the range of water-
175 surface wavelengths and heights in an absolute sense. In a relative sense, the change in the ranges
176 of clay content is similar, because the powers of d_0 and D_{50} are similar (eq. (B2), for $D_{50} < 0.5$ mm,
177 and eq. (10a)), but this will not be the case for $D_{50} > 0.5$ mm. Also, the measured L and h are not
178 within the $C_0 = 7.4\%$ range (Figure B1b). As L and h are below the threshold curve, this would
179 imply that ripples of this size are relict for this clay content. This is inconsistent with the
180 experimental results, since Wu et al. (2024) showed no reduction in λ_e for $C_0 \leq 7.4\%$.

181 ## 4.2 Doucette (2000), medium-sand field data

182 Doucette's (2000) field measurements were taken on a microtidal beach of Wambro Sound (run
183 1) where $h = 0.47$ m, $H = 0.2$ m and $T = 5.6$ s ($L = 11.9$ m), corresponding to $d_0 = 0.79$ m. The bed
184 was composed of medium sand, with $D_{50} = 0.22$ mm ($\theta_0 = 0.045$), and the measured ripples had a
185 wavelength of $\lambda_e = 250$ mm. Since $d_0/D_{50} = 3591$, the ripples were in the suborbital range (see
186 section 2.2), where the wavelength is dependent on both the orbital and grain diameters. Notice
187 this wavelength is above Diem's (1985) 200-mm limit. The supporting information demonstrates
188 that, whilst using Sleath's (1975) predictor for $C_0 = 0$ produces a difference, it is similar to the
189 other two example cases, which are below Diem's (1985) limit, and so is not considered
190 significant. From interpolation, P_θ in eq. (9) is determined to be 10. Figure 2b shows $L_{t\infty}$ and $AL_{t\infty}$
191 versus C_0 and Figure 2e shows the L–h phase space, for $C_0 = 0$, 7.4 and 16.3%. These reveal similar
192 behaviour to that of the coarse-grained sand case, but less extreme: in Figure 2b, $L_{t\infty}$ is still at its
193 minimum at $C_0 = 7.4\%$ and $AL_{t\infty}$ shows the same enhancement as in Figure 2a. The reduction in
194 range between the largest and smallest ($C_0 = 0\%$ and 7.4%) is by a factor of 2 for both the water-
195 surface wavelength and water depth (Figure 2e). Again, the actual surface wavelength and water
196 depth ($L = 11.9$ m, $h = 0.47$ m) are within all three ranges.

197 ## 4.3 Boyd et al. (1988), fine-sand field data

198 Boyd et al.'s (1988) field measurements were undertaken about 1 km from Martinique Beach on
199 the Atlantic coast of Nova Scotia during a period of relative calm (day 167, hour 9) where $h = 10$
200 m, $H = 0.5$ m and $T = 6.2$ s ($L = 50.7$ m), corresponding to $d_0 = 0.32$ m. The bed was composed of
201 well-sorted fine sand, with $D_{50} = 0.11$ mm ($\theta_0 = 0.076$), and the measured ripples had a wavelength
202 of $\lambda_e = 180$ mm. $d_0/D_{50} = 2873$ puts the ripples into the suborbital range. Assuming that P_θ in eq.
203 (9) is the same as for 0.143 mm ($P_\theta = 6.3$), Figure 2c shows $L_{t\infty}$ and $AL_{t\infty}$ versus C_0 and Figure 2f

shows the L–h phase space, for $C_0 = 0$, 7.4 and 16.3%. $L_{t\infty}$ in Figure 2c is still at its minimum at $C_0 = 7.4$%, but, because of far weaker clay enhancement of the threshold for fine sands in eq. (9), $L_{t\infty}$ is largest for $C_0 = 16.3$%. In Figure 2f, the measured water-surface wavelength and water depth ($L = 50.7$ m, $h = 10$ m) are below the threshold curve and outside the range for the $C_0 = 0$ and 7.4% clay contents, and just above the threshold curve and within range for $C_0 = 16.3$%, because, unlike the previous cases, $C_0 = 16.3$% produces the largest $L_{t\infty}$. Since there was little clay at the field site, the wave conditions were probably below threshold, implying that the observed ripples were relict. This is supported by the fact that Boyd et al.'s (1988) previous observation at day 167, hour 3, showed the same wavelength and no ripple migration. The reduction in range between the largest and smallest ($C_0 = 16.3$% and 7.4%) is again by a factor of 2 for both the water-surface wavelength and water depth (Figure 2f).

5 Discussion

The range of L shown in Figure 2 is largely controlled by $L_{t\infty}$, so it is of interest to determine how the change in clay content affects $L_{t\infty}$, eq. (10b), compared to the original clean-sand Diem method using Komar and Miller (1973), $L_{t\infty KM}$, eq. (B2) with $C_0 = 0$%. The net effect is shown as a ratio in Figure 3 for $C_0 = 0$, 7.4 and 16.3% and $0.1 \leq D_{50} \leq 0.8$ mm, for the approximate limits in the range of λ_e/D_{50} of 250 and 1,000. There are two competing effects: the reduction because of clay content (Figure 2) and the increase because of using Soulsby's (1997) threshold condition rather than Komar and Miller's (1973). Figure 3 shows a discontinuity for clean sand at $D_{50} = 0.5$ mm as a result of eq. (B2), leading to the largest difference ($L_{t\infty}$ is increased by up to 161% for $\lambda_e/D_{50} = 250$), which decreases with increasing λ_e/D_{50} (although Diem's (1985) method has rarely been applied for $D_{50} > 0.5$ mm). Otherwise for $D_{50} \leq 0.19$ mm, $L_{t\infty}$ is reduced by up to 36%, and for $0.19 < D_{50} \leq 0.5$ mm, $L_{t\infty}$ is increased by up to 64%. For $C_0 = 7.4$%, $L_{t\infty}$ is consistently decreased by between 35 and 56%, and for $C_0 = 16.3$%, $L_{t\infty}$ varies only slightly (increased by up to 14%, for $0.12 \leq D_{50} \leq 0.37$ mm, and otherwise reduced by up to 15%). The absence of a discontinuity in the present formulation, compared to Diem's (1985) original formulation, is clearly preferable. Also, the net effect of the clay on $L_{t\infty}$ will be stronger for smaller than for larger clay contents.

It is important to clarify how a representative clay content, C_0, for the ripples should be determined. In the modern environment this usually involves measuring C_0 below the active layer (below trough level), as efficient winnowing often removes clay from the body of the ripples during development (Wu et al., 2022). In the geological record, clay content in deposits should be based on primary clay minerals and diagenetic alterations for which it can be established that the original mineral was part of the primary clay fraction.

6 Conclusions

Preserved sedimentary bedforms provide important information for reconstructing past hydraulics in subaqueous environments by inverting bedform predictors, but this is usually based exclusively on non-cohesive sand. The present work incorporates the effects of sand-clay mixtures on bedforms, using the experimental results of Wu et al. (2024) in the non-cohesive inversion method of Diem (1985). Based on wave breaking and threshold of motion limitations, Diem's (1985) approach results in ranges for wave conditions. Here we have shown that the inclusion of as little as 7.4% clay in the most extreme case of coarse sand, $D_{50} \geq 0.45$ mm, reduces the possible ranges of water-surface wavelengths and water depths by factors of 3 and 4, respectively. For fine sand, the ranges are reduced by a factor of two. In short, not accounting for the modifying effect of clay

247   in ripple growth and equilibrium geometries, may lead to underestimating the prevailing flow
248   conditions if clay is present.

Appendix A: Determination of U_t^2 based on Soulsby (1997)

250   According to Soulsby (1997), the Shields parameter for the critical threshold of motion of clean
251   sand is

$$\theta_0 = \frac{0.3}{1+1.2D_*} + 0.055(1-e^{-0.02D_*}), \tag{A1}$$

252   where $D_* = [(s-1)g/\nu^2]^{1/3}D_{50}$, $s = \rho_s/\rho$, ρ_s and ρ are the water and sediment densities and ν is the
253   kinematic viscosity ($\sim$ 1 mm^2 s^{-1}). For waves, $\theta_0 = f_w U_t^2/2(s-1)gD_{50}$, where $f_w = 1.39(6d_0/D_{50})^{-0.52}$
254   is the skin friction factor (Soulsby et al., 1993). Rearranging the θ_0 wave expression gives U_t^2 as

$$U_t^2 = B(gd_0^{0.52}D_{50}^{0.48}), \tag{A2}$$

255   where $B = 6^{0.52}(s-1)\theta_0/0.695 = 3.653(s-1)\theta_0$. Eq. (A2) can be compared with eq. (B1).

Appendix B: Diem's (1985) threshold of motion constraint

257   Diem (1985) used the Komar & Miller (1973) expression for U_t^2, namely

$$U_t^2 = (s-1)g \times \begin{cases} 0.21(d_0^{0.5}D_{50}^{0.5}), & D_{50} < 0.5 \text{ mm}, \\ 0.46\pi(d_0^{0.25}D_{50}^{0.75}), & D_{50} \geq 0.5 \text{ mm}, \end{cases} \tag{B1}$$

258   such that with the inclusion of clay $L_{t\infty} = \pi g d_0^2/2B_\theta U_t^2$, $d_0 = \lambda_e/\alpha$ and B_θ and α are given by eqs. (8)
259   and (9), giving $L_{t\infty}$ as

$$L_{t\infty} = \frac{\pi}{2(s-1)} \times \begin{cases} \dfrac{1}{0.21[B_\theta\alpha^{1.5}]}\left(\dfrac{\lambda_e^{1.5}}{D_{50}^{0.5}}\right), & D_{50} < 0.5 \text{ mm}, \\ \dfrac{1}{0.46\pi[B_\theta\alpha^{1.75}]}\left(\dfrac{\lambda_e^{1.75}}{D_{50}^{0.75}}\right), & D_{50} \geq 0.5 \text{ mm}, \end{cases} \tag{B2}$$

260   and $AL_{t\infty}$ as $\lambda_e/0.142[\alpha]$ remains the same. Figure B1 shows the effect of this parameterisation of
261   the threshold of motion for the first example case of Wu et al. (2018) depicted in Figures 2a,d.
262   Unlike Figure 2d, the measured values of h and L are outside the range predicted for $C_0 = 7.4\%$.

Open Research

269   Eqs. (8) and (9) are from Wu et al. (2024), which has its own open-access policy.

References

271   Allen, P.A. (1981). Some guidelines in reconstructing ancient sea conditions from wave
272   ripplemarks. *Marine Geology*, *43*, 59–67. https://doi.org/10.1016/0025-3227(81)90176-6

Allen, P.A., & Hoffman, P.F. (2005). Extreme winds and waves in the aftermath of a Neoproterozoic glaciation. *Nature*, *433*, 123–127. https://doi.org/10.1038/nature03176

Aspler, L.B., Chiarenzelli, J.R., & Bursey, T.L. (1994). Ripple marks in quartz arenites of the Hurwitz group, Northwest territories, Canada: evidence for sedimentation in a vast, early Proterozoic, shallow, fresh-water lake. *Journal of Sedimentary Research*, *A64*, 282–298. https://doi.org/10.1306/D4267D7F-2B26-11D7-8648000102C1865D

Baas, J.H. (1994). A flume study on the development and equilibrium morphology of current ripples in very fine sand. Sedimentology, *41*, 185–209. https://doi.org/10.1111/j.1365-3091.1994.tb01400.x

Boyd, R., Forbes, D.L., & Heffler, D.E. (1988). Time-sequence observations of wave-formed sand ripples on an ocean shoreface. *Sedimentology*, *35*, 449–464. https://doi.org/10.1111/j.1365-3091.1988.tb00997.x

Collinson, J., & Mountney, N. (2019). *Sedimentary structures* (Fourth Edition), Edinburgh, UK: Dunedin Academic Press. ISBN 1780460627

Cuadrado, D.G. (2020). Geobiological model of ripple genesis and preservation in a heterolithic sedimentary sequence for a supratidal area. *Sedimentology*, *67*, 2747–2763. https://doi.org/10.1111/sed.12718

Davies, N.S., Liu, A.G., Gibling, M.R., & Miller, R.F. (2016). Resolving MISS conceptions and misconceptions: A geological approach to sedimentary surface textures generated by microbial and abiotic processes. *Earth-Science Reviews*, *154*, 210–246. https://doi.org/10.1016/j.earscirev.2016.01.005

Diem, B. (1985). Analytical method for estimating palaeowave climate and water depth from wave ripple marks. *Sedimentology*, *32*, 705–720. https://doi.org/10.1111/j.1365-3091.1985.tb00483.x

Doucette, J.S. (2000). The distribution of nearshore bedforms and effects on sand suspension on low-energy, micro-tidal beaches in Southwestern Australia. *Marine Geology*, *165*, 41–61. https://doi.org/10.1016/S0025-3227(00)00002-5

Komar, P.D., & Miller, M.C. (1973). The threshold of sediment movement under oscillatory water waves. *Journal of Sedimentary Petrology*, *43*, 1101–1110. https://doi.org/10.1306/74D7290A-2B21-11D7-8648000102C1865D

Lamb, M.P., Fischer, W.W., Raub, T.D., Perron, J.T., & Myrow, P.M. (2012). Origin of giant wave ripples in snowball Earth cap carbonate. *Geology*, *40*, 827–830. https://doi.org/10.1130/G33093.1

Malarkey, J., Baas, J.H., Hope, J.A., Aspden, R.J., Parsons, D.R., Peakall, J., Paterson, D.M., Schindler, R.J., Ye, L., Lichtman, I.D., Bass, S.J., Davies, A.G., Manning, A.J., & Thorne, P.D. (2015). The pervasive role of biological cohesion in bedform development. *Nature communications*, *6*, 6257. https://doi.org/10.1038/ncomms7257

Malarkey, J., & Davies, A.G. (2003) A non-iterative procedure for the Wiberg and Harris (1994) oscillatory sand ripple predictor. *Journal of Coastal Research*, *19*, 738-739. http://www.jstor.org/stable/4299210

Miche, R. (1944). Mouvements ondulatoires de la mer en profondeur constante ou décroissante. *Annales des Ponts et Chaussées*, *19*, 369–406. https://repository.tudelft.nl/islandora/object/uuid%3A6fceef55-d71b-4e3e-a94f-98ff17cb8f91

Miller, M.C., & P.D. Komar (1980). Oscillation sand ripples generated by laboratory apparatus. *Journal of Sedimentary Petrology*, *50*, 173–182. https://doi.org//10.1306/212F799B-2B24-11D7-8648000102C1865D

Mogridge, G.R., Davies, M.H., & Willis, D.H. (1994). Geometry prediction for wave-generated bedforms. *Coastal Engineering*, *22*, 255–286. https://doi.org/10.1016/0378-3839(94)90039-6

Parsons, D.R., Schindler, R.J., Hope, J.A., Malarkey, J., Baas, J.H., Peakall, J., Manning, A.J., Ye, L., Simmons, S., Paterson, D.M., Aspden, R.J., Bass, S.J., Davies, A.G., Lichtman, I.D., & Thorne, P.D. (2016). The role of biophysical cohesion on subaqueous bed form size. *Geophysical Research Letters*, *43*, 1566–1573. https://doi.org/10.1002/2016GL067667

Pedocchi, F., & García, M.H. (2009). Ripple morphology under oscillatory flow: 2. Experiments, *Journal of Geophysical Research*, *114*, C12015. https://doi.org/10.1029/2009JC005356

Perron, J.T., Myrow, P.M., Huppert, K.L., Koss, A.R., & Wickert, A.D. (2018). Ancient record of changing flows from wave ripple defects. *Geology*, *46*, 875–878. https://doi.org/10.1130/G45463.1

Pochat, S., & Van Den Driessche, J. (2011). Filling sequence in Late Paleozoic continental basins: A chimera of climate change? A new light shed given by the Graissessac–Lodève basin (SE France). *Palaeogeography, Palaeoclimatology, Palaeoecology*, *302*, 170–186. https://doi.org/10.1016/j.palaeo.2011.01.006

Sleath, J.F.A. (1975). A contribution to the study of vortex ripples. *Journal of Hydraulic Research*, *13*, 315–328. https://doi.org/10.1080/00221687509499705

Soulsby, R. (1997). *Dynamics of Marine Sands: A Manual for Practical Applications*, London UK: Thomas Telford. ISBN 072772584X

Soulsby, R.L., Hamm, L., Klopman, G., Myrhaug, D., Simons, R.R., & Thomas, G.P. (1993). Wave–current interactions within and outside the bottom boundary layer. *Coastal Engineering*, 21, 41–69. https://doi.org/10.1016/0378-3839(93)90045-A

Vignaga, E., Sloan, D.M., Luo, X., Haynes, H., Phoenix, V.R., & Sloan, W.T. (2013). Erosion of biofilm-bound fluvial sediments. *Nature Geoscience*, *6*, 770–774. https://doi.org/10.1038/ngeo1891

Wetzel, A., Allenbach, R., & Allia, V. (2003). Reactivated basement structures affecting the sedimentary facies in a tectonically "quiescent" epicontinental basin: an example from NW Switzerland. *Sedimentary Geology*, *157*, 153–172. https://doi.org/10.1016/S0037-0738(02)00230-0
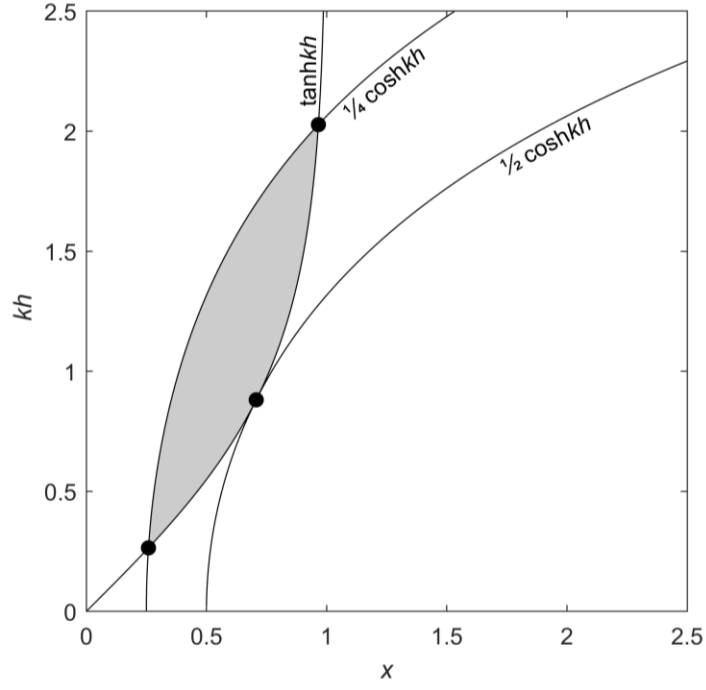
Whitehouse, R., Soulsby, R., Roberts W., & Mitchener, H. (2000). *Dynamics of estuarine muds: A Manual for Practical Applications*, London UK: Thomas Telford. ISBN 0727728644

Wiberg, P.L., & Harris, C.K. (1994). Ripple geometry in wave-dominated environments. *Journal of Geophysical Research*, *99*(C1), 775–789. https://doi.org/10.1029/93JC02726

Wu, X., Baas, J.H., Parsons, D.R., Eggenhuisen, J., Amoudry, L., Cartigny, M., McLelland, S., Mouazé, D., & Ruessink, G. (2018). Wave ripple development on mixed clay–sand substrates: Effects of clay winnowing and armoring. *Journal of Geophysical Research: Earth Surface*, *123*, 2784–2801. https://doi.org/10.1029/2018JF004681

Wu, X., Fernández, R., Baas, J.H., Malarkey, J., & Parsons, D.R. (2022). Discontinuity in equilibrium wave–current ripple size and shape and deep cleaning associated with cohesive sand–clay beds. *Journal of Geophysical Research: Earth Surface*, *127*, e2022JF006771. https://doi.org/10.1029/2022JF006771

Wu, X., Malarkey, J., Fernández, R., Baas, J.H., Pollard, E., & Parsons, D.R. (2024). Influence of cohesive clay on wave-current ripple dynamics captured in a 3D phase diagram. *Earth Surface Dynamics*, *12*, 231–247. https://doi.org/10.5194/esurf-12-231-2024

Figure 1 *kh* versus *x* ($L/L_{t\infty}$) for the limiting case of $A = \frac{1}{2}$ and also $A = \frac{1}{4}$. Dots correspond to $x = 2^{-\frac{1}{2}}$ and $kh = \text{arctanh}\,2^{-\frac{1}{2}}$, for $A = \frac{1}{2}$; $x_{max,min} = \frac{1}{2}(2\pm3^{\frac{1}{2}})^{\frac{1}{2}}$ and $kh_{max,min} = \text{arctanh}[x_{max,min}]$, for $A = \frac{1}{4}$, and shading represents allowable values of x and kh for $A = \frac{1}{4}$ ($\frac{1}{4}\cosh kh \leq x \leq \tanh kh$).
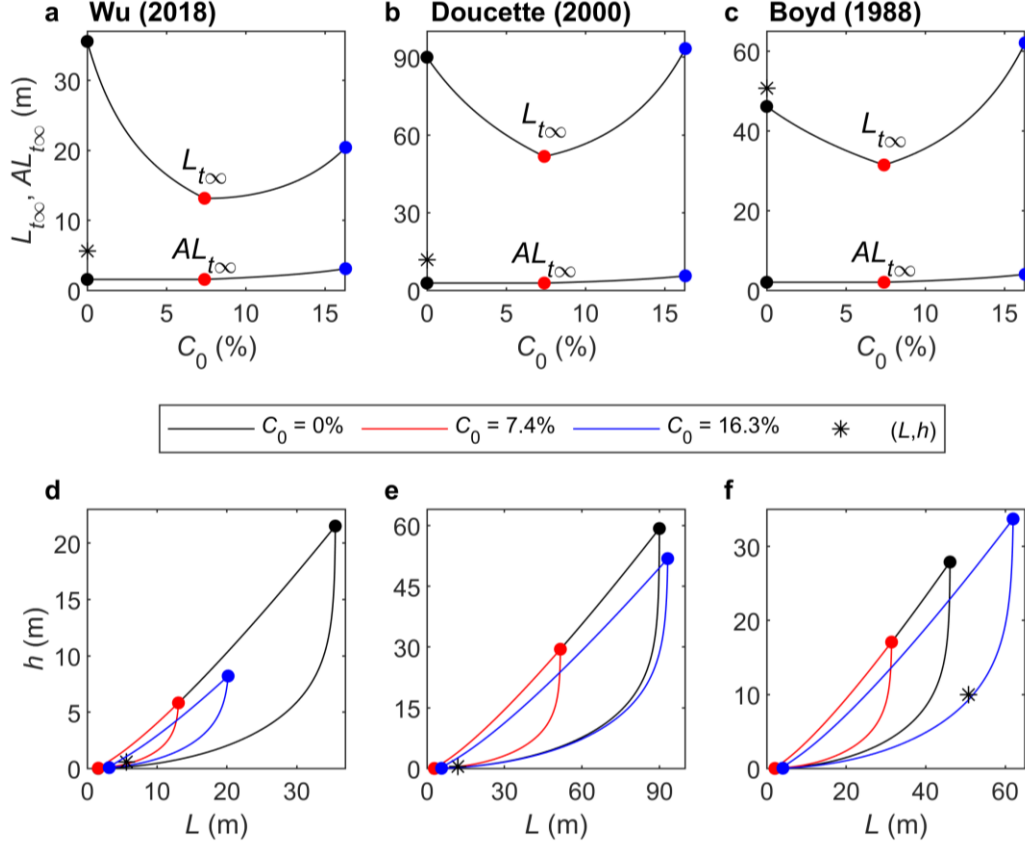
Figure 2 (a,b,c) Threshold, $L_{t\infty}$, and wave-breaking, $AL_{t\infty}$, scales, eqs. (10b,c), versus C_0 and (d,e,f) L–h phase space from eq. (5), showing the different ranges for $C_0 = 0$, 7.4 and 16.3% and the measured L and h. For (a,d) Wu et al. (2018), $\lambda_e = 278D_{50}$, $D_{50} = 0.496$ mm, $\theta_0 = 0.032$, $L = 5.62$ m and $h = 0.6$ m; for (b,e) Doucette (2000), $\lambda_e = 250$ mm, $D_{50} = 0.22$ mm, $\theta_0 = 0.045$, $L = 11.9$ m and $h = 0.47$ m, and for (c,f) Boyd et al. (1988), $\lambda_e = 180$ mm, $D_{50} = 0.11$ mm, $\theta_0 = 0.076$, $L = 50.7$ m and $h = 10$ m. Legend applies to d,e,f; colours in a,b,c are consistent with the legend.
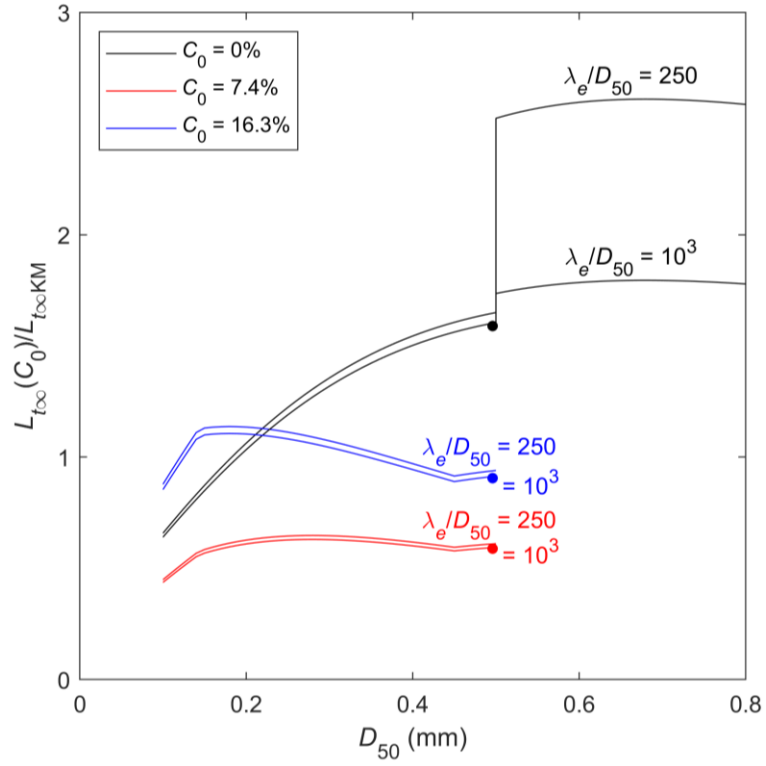
Figure 3 Relative size of $L_{t\infty}(C_0)$ from eq. (10b) normalised by the clean-sand $L_{t\infty}$ from eq. (B2), $L_{t\infty KM}$, for $C_0 = 0$, 7.4 and 16.3%. $\lambda_e/D_{50} = 250$ and 1000, and the dots correspond to Wu et al.'s (2018) clean-sand experiment in Figure 2a.
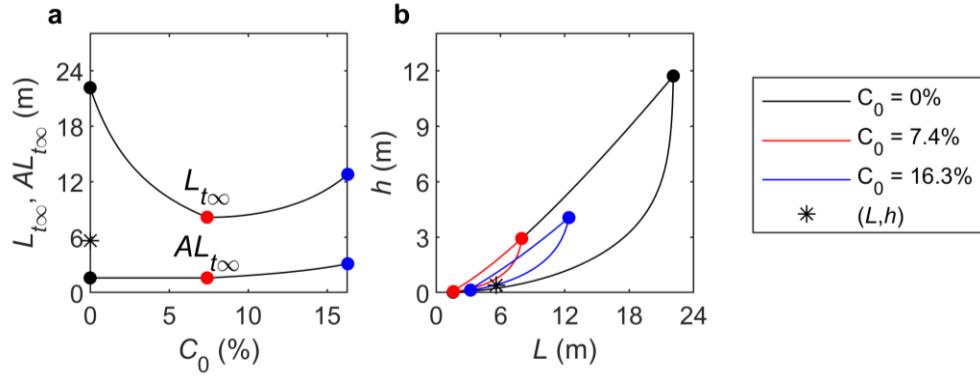
Figure B1 (a) Threshold, $L_{t\infty}$, and wave-breaking scales, $AL_{t\infty}$, eqs. (B2) and (10c), versus C_0 and (b) L–h phase space from eq. (5) showing the different ranges for $C_0 = 0$, 7.4 and 16.3% and the measured h and L for Wu et al. (2018), $\lambda_e = 278D_{50}$, $D_{50} = 0.496$ mm, $h = 0.6$ m and $L = 5.62$ m.